

www.acsanm.org Article

# In Situ Tensile Testing of Nanometer-Thick Two-Dimensional Transition-Metal Carbide Films: Implications for MXenes Acting as Nanoscale Reinforcement Agents

Yanxiao Li, Longjie Wei, Shuohan Huang, Arman Ghasemi, Wei Gao, Chenglin Wu,\* and Vadym N. Mochalin\*



Cite This: ACS Appl. Nano Mater. 2021, 4, 5058-5067



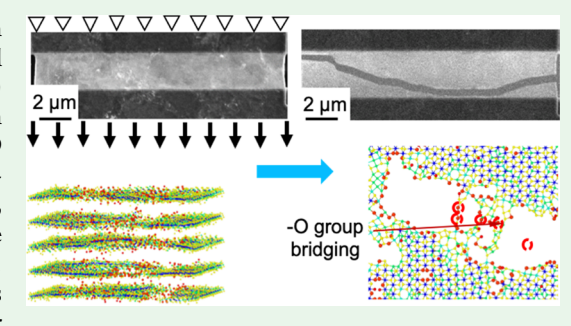
ACCESS

Metrics & More

Article Recommendations

Supporting Information

**ABSTRACT:** In-plane mechanical behavior of stacks formed by titanium carbide MXenes ( $\mathrm{Ti_2CT}_x$ ,  $\mathrm{Ti_3C_2T}_x$ ) was investigated in a microscale uniaxial tensile experiment with the *in situ* scanning electron microscope (SEM) nanoindenter and a push-to-pull (PTP) micro-electro-mechanical system (MEMS). When the number of MXene monolayers in a stack varies from 9 to 26 ( $\mathrm{Ti_2CT}_x$  with *d*-spacing of 1.36 nm) and 7 to 52 ( $\mathrm{Ti_3C_2T}_x$  with *d*-spacing of 1.48 nm), the measured Young's moduli stay almost constant, averaging at 217.75 GPa ( $\mathrm{Ti_2CT}_x$ ) and 204.92 GPa ( $\mathrm{Ti_3C_2T}_x$ ). In the same experiment, the measured tensile strength monotonically decreases from 9.61 to 7.59 GPa ( $\mathrm{Ti_2CT}_x$ ) and 9.89 to 7.99 GPa ( $\mathrm{Ti_3C_2T}_x$ ). Notably, this dependence on the number of stacked MXene monolayers is much weaker



than that previously observed in multilayer graphene and MoS<sub>2</sub> stacks, which displayed a significant reduction of both tensile strength and Young's modulus, compared to what was expected from additivity, as the number of monolayers increased. This difference implies a better scaling-up of the mechanical properties of MXenes as compared to other multilayer two-dimensional (2D) materials. Furthermore, atomistic simulations show that defects in different layers in the multilayer MXenes give rise to the observed dependence of the tensile strength on the number of MXene monolayers in a stack. The atomic damage initiated in the weakest layer with the highest defect density promotes strain softening, leading to a reduced tensile strength of the MXenes. Our results show that multilayer MXenes could be used as excellent mechanical reinforcing agents for composite materials across scales and potentially in other applications where robust mechanical performance is essential.

KEYWORDS: in situ tensile testing, MXenes, Young's modulus, tensile strength, number-of-layer dependency

# **■ INTRODUCTION**

MXenes, a large family of transition-metal carbides and carbonitrides, are synthesized by treatment of Al-containing MAX phases<sup>1,2</sup> with a formula  $M_{n+1}AX_n$ , where "M" is an early transition metal, "A" is an A-group element (mostly groups 13 and 14), "X" is carbon or nitrogen, and n=1, 2, 3, etc., 3,4 in aqueous hydrofluoric acid (HF) solutions leading to selective etching of Al. 5,6 The resulting stacked  $M_{n+1}X_n$  layers are terminated with mostly oxygen- and/or fluorine-containing groups. These terminated MXenes are referred to as  $M_{n+1}X_nT_{xy}$  where T represents the terminating groups, x is their fraction in the formula.

 ${
m Ti_2CT_x}$  and  ${
m Ti_3C_2T_x}$  are the two most experimentally investigated MXenes. They have demonstrated excellent electrochemical performance and promising potential in Liion batteries, 12,13 supercapacitors, 14,15 optoelectronics, 16–19 Terahertz (THz) electromagnetic interference (EMI) shielding and communications, 20–22 catalysis, 23–26 and sensors. 27–30 Recent experimental demonstrations of MXene suprelubricity and superior wear resistance 32 on the macroscale are

especially important for lubrication and antiwear applications. MXenes were also reported as reinforcing agents for composites. Specifically, much more tunable mechanical properties of double transition-metal MXenes were found in comparison with graphene. Mechanical properties of MXenes, although receiving an increased attention in the past few years, Avenue may be not been systematically studied yet.

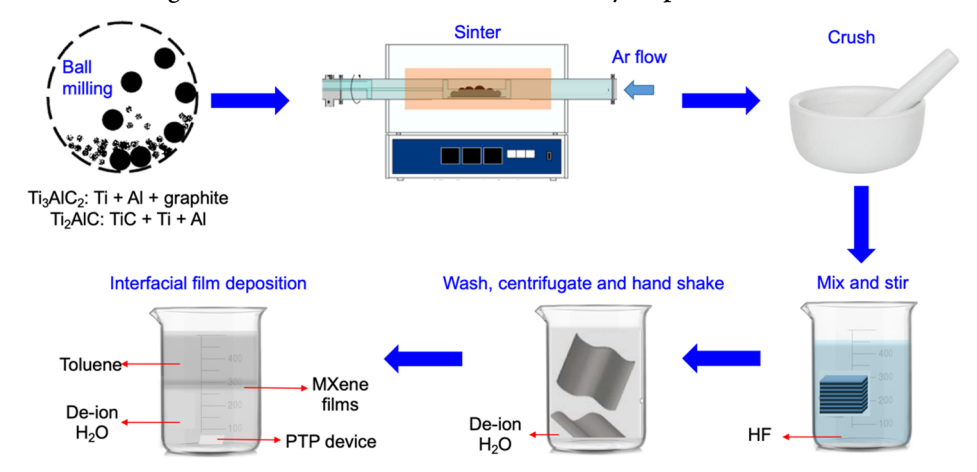
Two-dimensional (2D) materials have a high in-plane Young's modulus, strength, and adhesion. However, for very thin materials, such as graphene, these properties are increasingly sensitive to defects and depend on the number of layers stacked in the sample. <sup>44,45</sup> A recent study on adhesion of MXenes has shown that the number-of-layer dependence of

Received: February 20, 2021 Accepted: April 29, 2021 Published: May 13, 2021





Scheme 1. Synthesis and Etching of MAX Phases to MXenes Followed by Deposition of MXene Films on PTP Devices



adhesion energy is negligible for MXenes, which was attributed to their thicker monolayers as compared to graphene. <sup>46</sup> Atomic force microscopy (AFM) indentation experiments have shown a high Young's modulus  $(0.33 \pm 0.03 \text{ TPa})^{37}$  for monolayer  $\text{Ti}_3\text{C}_2\text{T}_x$  MXene. It is interesting now to investigate the number-of-layer dependence and defect tolerance of the inplane mechanical properties of MXenes, which remain unknown.

In this paper, the mechanical properties of monolayer to multilayer MXene films are investigated at the nano- to micrometer scale via in situ tensile testing and atomistic simulations. Experimental results show that Young's modulus exhibits only a small variance when the number of stacked MXene monolayers increases from 9 to 26 for Ti<sub>2</sub>CT<sub>r</sub> or 7 to 52 for Ti<sub>3</sub>C<sub>2</sub>T<sub>x</sub>. Meanwhile, the tensile strength monotonically decreases from 9.61 to 7.59 GPa (for Ti<sub>2</sub>CT<sub>x</sub> with d-spacing of 1.36 nm) and from 9.89 to 7.99 GPa (for Ti<sub>3</sub>C<sub>2</sub>T<sub>x</sub> with dspacing of 1.48 nm). Comparing with what was previously observed in multilayer graphene and MoS2, this dependence on the number of stacked monolayers is much weaker, implying good scaling-up of mechanical properties of the tested MXenes. The dependence on the number of monolayers in a stack can be attributed to variations in the number of atomic vacancies among different monolayers in the multilayer MXenes, as revealed by our atomistic simulations. Molecular dynamics (MD) simulations have also demonstrated that the cracks in the MXene flakes can be bridged by the -O- atoms, hindering their propagation and leading to a ductile failure behavior nontypical for ceramics.

# MATERIALS AND METHODS

Synthesis of MXenes and Fabrication of MXene Films. MAX phases were chemically converted to MXene films, and MXene films were deposited onto push-to-pull (PTP) devices (Scheme 1). The details are as follows. Etching of  $Ti_2AlC$  and  $Ti_3AlC_2$  MAX phases was performed according to the previous report. Ti\_2AlC was synthesized by mixing TiC (typically 2  $\mu$ m size, 99.5%, Alfa Aesar), Ti (-325 mesh, 99%, Alfa Aesar), and Al (-325 mesh, 99.5%, Alfa Aesar) powders in a 0.85:1.15:1.05 molar ratio for 12 h and heating at 10 °C/min from room temperature to 1400 °C for 4 h under Ar flow. Ti\_3AlC\_2 was synthesized by mixing Ti, Al, and graphite (-325 mesh, 99%, Alfa Aesar) powders in a 3:1.1:1.88 molar ratio for 12 h and heating at 10 °C/min from room temperature to 1550 °C for 2 h under Ar flow. The resulting MAX phase ceramics were manually crushed in a mortar by a pestle and sieved through a -325 mesh sieve.

The MAX phases were chemically converted to MXenes (Scheme 2). Ti<sub>2</sub>CT<sub>x</sub> was synthesized by slowly adding 0.3 g of Ti<sub>2</sub>AlC to the

# Scheme 2. Commonly Accepted Chemical Reactions in MXene Synthesis

$$LiF + HCl = HF + LiCl$$
 (1)

$$Ti_3AlC_2 + 3HF = AlF_3 + \frac{3}{2}H_2\uparrow + Ti_3C_2$$
 (2)

$$Ti_2AIC + 3HF = AIF_3 + \frac{3}{2}H_2\uparrow + Ti_2C$$
 (3)

etchant prepared by dissolving 0.3 g of LiF in 3 mL of 9 M HCl in a plastic centrifuge tube. The etching reaction was carried out for 36 h at 35 °C.  $\rm Ti_3C_2T_x$  was synthesized by slowly adding 0.3 g of  $\rm Ti_3AlC_2$  to the etchant prepared by dissolving 0.3 g of LiF in 3 mL of 9 M HCl in a plastic centrifuge tube. The etching duration was 36 h at 35 °C. The etched powder was washed with DI water several times until the pH of the supernatant reached  $\sim$ 6. After this, MXene colloidal solutions were obtained *via* 5 min of handshaking followed by 1 h of centrifugation at 3500 rpm.

MXene thin films of different thicknesses were deposited on PTP devices following the procedures in our previous study. 46 In brief, 20-200  $\mu$ L of as-prepared Ti<sub>2</sub>CT<sub>x</sub> colloidal solution was mixed with 4–8 mL of toluene in 50 mL of water, and the dispersion was poured into a beaker containing 400 mL of water, leading to the formation of a Ti<sub>2</sub>CT<sub>x</sub> thin film at the interface between the water and toluene phases. The PTP device was then lifted up slowly through the interface catching the Ti<sub>2</sub>CT<sub>x</sub> film. Ti<sub>3</sub>C<sub>2</sub>T<sub>x</sub> films were prepared using the same method with 20-100  $\mu$ L of Ti<sub>3</sub>C<sub>2</sub>T<sub>x</sub> colloidal solution. Finally, the MXene films on PTP devices were dried in an ambient environment before testing. By adjusting the concentration of colloidal solution during sample preparation, Ti<sub>2</sub>CT<sub>x</sub> films with a different number of monolayers (9, 12, 26) and Ti<sub>3</sub>C<sub>2</sub>T<sub>x</sub> films with 7, 9, 13, 32, and 52 monolayers were deposited. Raman spectra of  $Ti_2CT_x$  and  $Ti_3C_2T_x$  prepared by the above techniques can be found in our previous study<sup>46</sup> and are shown in Figure S1a, Supporting Information (SI)

*In Situ* Tensile Testing. The microscale uniaxial tensile experiment was enabled by the *in situ* scanning electron microscope (SEM) (Helios NANO LAB 600) nanoindenter (PI 85 PicoIndenter, Hysitron, Inc., Minneapolis, MN) and a PTP device (PTP, Hysitron, Inc., Minneapolis, MN).

MD Modeling. Uniaxial tension of materials was performed along the zigzag direction, as shown in Figure 7. An MD run in the NVT ensemble at 25 °C was first conducted for equilibration. During the tension along the longitudinal direction, the atoms within 0.3 nm distance from the upper edge of the sample were moved up at a constant strain rate of 0.002 ps<sup>-1</sup>, while the atoms within the same

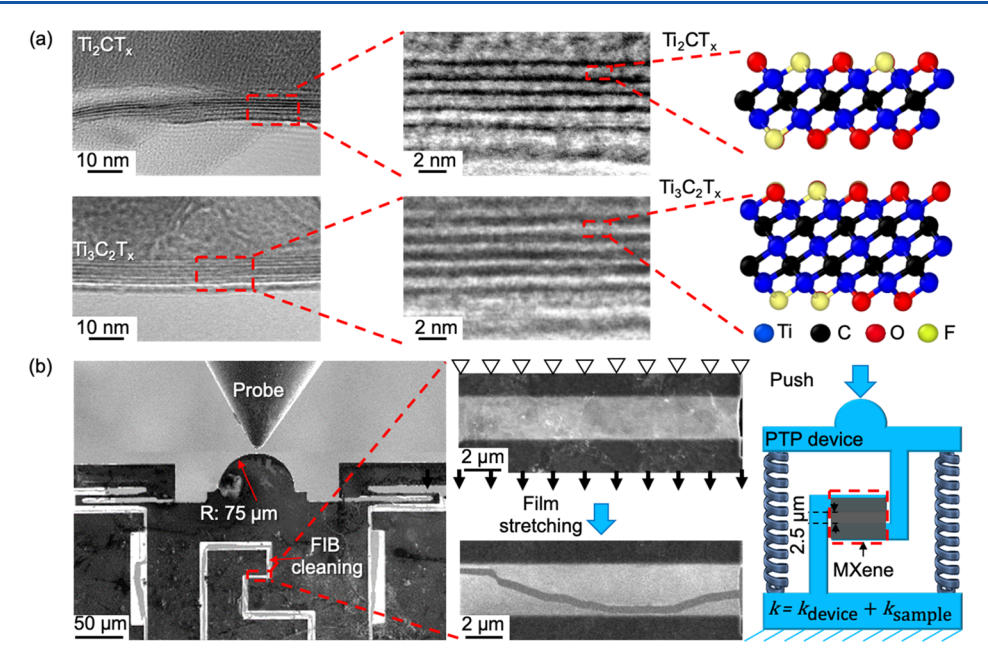


Figure 1. (a) TEM images of the MXene films and atomistic structures of  $Ti_2CT_x$  and  $Ti_3C_2T_x$ . (b) SEM images of a PTP device and nanoindenter (left) with  $Ti_3C_2T_x$  flakes (red dashed square) before and after stretching and a schematic of a push-to-pull MEMS device (right).

distance from the lower edge of the sample were kept fixed, simulating stretching of the sample. Periodic boundary conditions were applied along all three orthogonal directions (two in-plane and one out-of-plane) in the modeling, while 5 nm vacuum slabs were added along all directions to avoid possible interactions with the images of the atoms in neighboring cells due to the periodic boundary conditions. The strain—stress response, sample structure, and strain distribution were extracted and generated with Ovito<sup>48,49</sup> visualization software. Multibody stress definition is adopted for the overall and per-atom stress calculations, where boundary atoms are excluded.

**Vacancy Generation.** Initially, the Ti and C atoms are assigned with a unique number identifier ranging from 1 to the total number of atoms. A random sequence was generated following a uniform distribution function to remove the atoms and reach the 3.0% average vacancy ratio based on the published high-resolution transmission electron microscopy (HRTEM) measurements. The final generated vacancy ratio is  $3.0 \pm 0.5\%$  over an average area of 7.5 nm  $\times$  8.0 nm in the MD model.

**Terminating Group Generation.** The surface terminating group site occupation ratio,  $R_{\text{site,A}}$  (A = O or F for the terminating group type), is determined based on the following equation

$$R_{\text{site,A}} = \frac{R_{\text{XPS,A}} \times N_{\text{total}}}{N_{\text{site}}} \tag{4}$$

where  $R_{\rm XPS,A}$  is the ratio of the number of terminating groups to the total number of Ti and C atoms based on the X-ray photoelectron spectroscopy (XPS) results. <sup>46</sup>  $N_{\rm total}$  is the number of Ti and C atoms of defected MXene in MD modeling,  $N_{\rm site}$  is the number of surface terminating group sites, which are the locations where O, F, or other atoms could attach to the Ti layer as terminating groups. Afterward, the O or F atoms were added to the terminating group sites with the ratio of  $R_{\rm site,A}$ . The process follows the procedure described in the vacancy generation approach.

#### RESULTS AND DISCUSSION

In Situ Tensile Testing Results. SEM and transmission electron microscope (TEM) images of the MXene films are shown in Figure 1a. MXene films reported in literature are polycrystalline, several to hundreds of nanometers thick (depending on the number of monolayers in a stack).  $^{5,17}$  The in-plane stress—strain relationships for multilayer  $\mathrm{Ti}_2\mathrm{CT}_x$ 

and Ti<sub>3</sub>C<sub>2</sub>T<sub>x</sub> films were measured in a microscale uniaxial tensile experiment enabled by the in situ SEM, nanoindenter, and a push-to-pull (PTP) micro-electro-mechanical system (MEMS). The testing was carried out with the nanoindenter coupled to the PTP device, as shown in Figure S2 (SI), and operated with a SEM in a displacement-controlled mode at the 10 nm/s rate. The PTP device microfabricated on a silicon-oninsulator wafer consists of a semicircular end (75.00  $\mu$ m in diameter) and specially designed cutouts, as shown in Figure 1b. When pushed by a flat punch diamond probe (5.00  $\mu$ m in diameter) on the semicircular end, the initial 2.50 µm wide gap widens, leading to uniaxial stretching of the material suspended over this gap (Figure 1b). Before testing, MXene films were deposited on the loading device and parts of the films outside the gap region were removed by dual focused ion beam (FIB). During the in situ SEM tensile testing, a real-time video was recorded to analyze the deformation and failure mechanism, while the force-displacement data of the probe were measured by the nanoindenter. The force exerted on the flat punch is proportional to a sum of the stiffness of the PTP device and the sample, as schematically shown in Figure 1b, since the sample and PTP device springs share the same displacement.

The stress applied to the MXene film is defined as  $\sigma = \frac{F}{t \cdot w \cdot n}$ , where F is the measured force exerted on the film, t is the monolayer thickness of the MXene (1.36 nm for  $\text{Ti}_2\text{CT}_x$  and 1.48 nm for  $\text{Ti}_3\text{C}_2\text{T}_x$  monolayer thicknesses of MXenes were calculated from X-ray diffraction results, <sup>46</sup> as shown in Figure S1b, SI), w is the width of the film ( $\sim$ 17  $\mu$ m, *i.e.*, the dimension perpendicular to the loading direction, which is controlled by FIBing), and n is the number of layers in the stack determined by the averaged fringe count from TEM images, as shown in Figure S3 (SI) (details on determination of the number of layers are provided in Note S1, SI). The strain is defined as  $\varepsilon = \frac{D}{l}$ , where D is the displacement exerted on the film and l is the length of the suspended sample in the loading direction. The typical experimental stress—strain curves for  $\text{Ti}_2\text{CT}_x$  and

 $Ti_3C_2T_x$  films made of nine monolayers are compared in Figure 2.

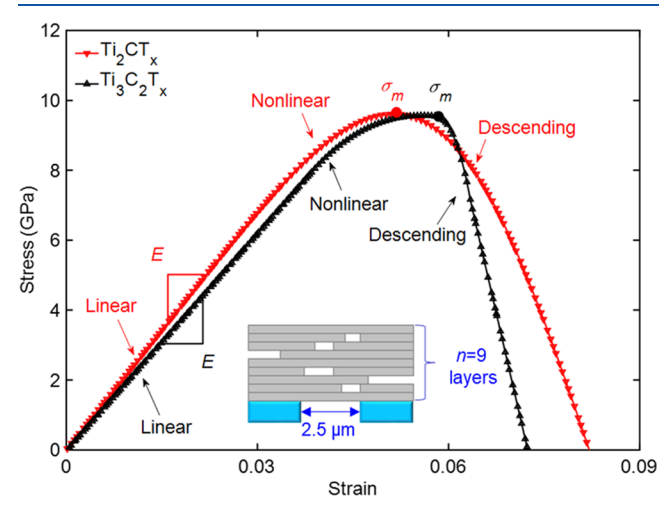


**Figure 2.** Stress—strain curves for nine-layer  $Ti_2CT_x$  and  $Ti_3C_2T_x$  samples. The inset illustrates the side view of the overlapping multilayered MXene film being stretched over the gap.

The corresponding deformations were captured by SEM images (Figure 3). Based on the stress–strain curves, the deformation responses for both MXenes can be divided into three stages: the linear stage, the nonlinear stage, and the stress descending stage, as shown in Figure 2. The linear stage corresponds to elastic deformation of the sample since no cracks were observed prior to  $\varepsilon = 0.034~(0.043)$  for  ${\rm Ti}_2{\rm CT}_x~({\rm Ti}_3{\rm C}_2{\rm T}_x)$ . The nonlinear stage partially comes from the

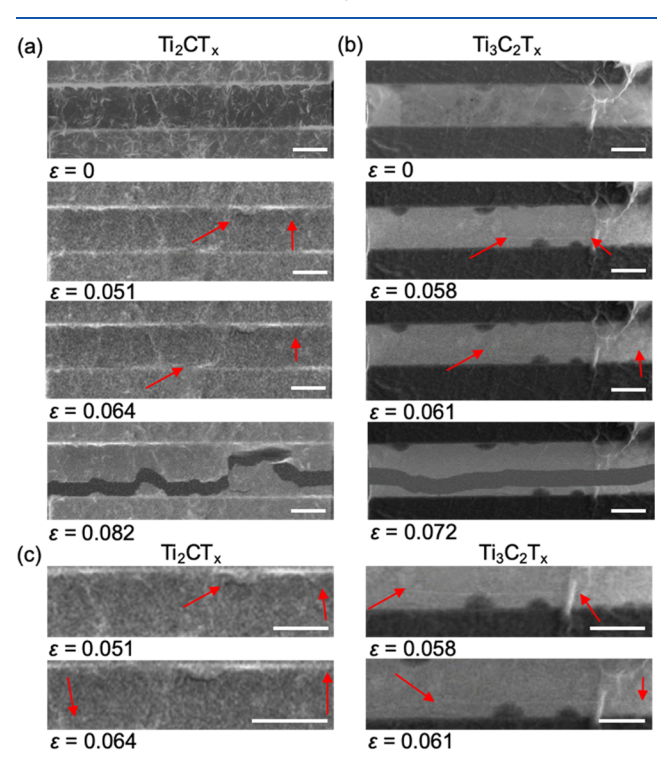


**Figure 3.** SEM images taken during the tensile testing of (a)  $\text{Ti}_2\text{CT}_x$  and (b)  $\text{Ti}_3\text{C}_2\text{T}_x$  samples at different values of applied strain  $(\varepsilon)$ . (c) Zoomed-in images of the crack. Red arrows show the beginning and end of cracks. Scale bars are 2  $\mu\text{m}$ .

nonlinear elastic behavior at the finite strain. Crack initiation was observed in SEM images (Figure 3) at  $\varepsilon=0.051$  (0.058) for nine-layer  ${\rm Ti_2CT_x}$  ( ${\rm Ti_3C_2T_x}$ ) with the maximum stress values  $\sigma_{\rm m}=9.61$  and 9.55 GPa. The cracks are indicated in SEM images by red arrows. This was followed by the stress descending stage caused by crack propagation. Eventually, the cracks propagated through the entire sample in the gap leading to failure at  $\varepsilon=0.082$  (0.072) for  ${\rm Ti_2CT_x}$  ( ${\rm Ti_3C_2T_x}$ ). The number of layers was determined after failure using a TEM (typical TEM images are shown in Figure 4, details on determining the number of layers are shown in Note S1, SI).

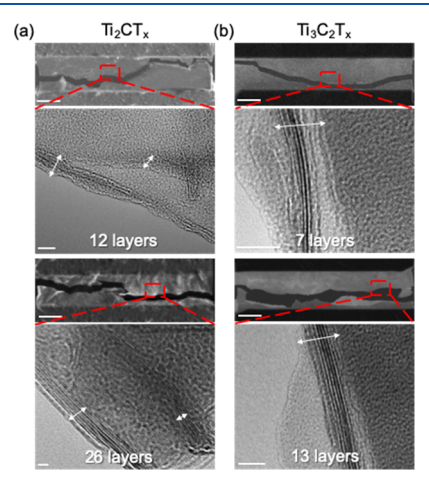


**Figure 4.** SEM (top) and the corresponding TEM (underneath) images of fractured MXene films made of a different number of layers: (a)  $\text{Ti}_2\text{CT}_x$  and (b)  $\text{Ti}_3\text{C}_2\text{T}_x$  flakes. Scale bars: 2  $\mu\text{m}$  for SEM images and 10 nm for TEM images.

The stress-strain curves for specimens with different numbers of stacked layers are compared in Figure 5. All of the curves exhibit a similar linear response. In the nonlinear stage, however, for the samples with more layers in the film, the material becomes softer beyond a certain strain, manifested by a reduced strength as compared to the monolayer case. This number-of-monolayer dependence has also been found in atomistic modeling results and corresponds to the situation when the failure of the multilayer system is initiated in the weakest monolayer and subsequently propagates to other layers, *i.e.*, it is a sequential layer-by-layer failure mechanism instead of a concerted failure of all monolayers in the structure. The failure mechanism at the atomistic scale is discussed in the following modeling section.

Our measured results for the two MXene samples are listed in Table 1 and compared with the literature data for MoS<sub>2</sub><sup>52</sup> and graphene<sup>53,54</sup> produced using a similar experimental setup in Table S1, SI. To compare the dependence of strength and Young's moduli of MXenes on the number of monolayers to similar dependencies for MoS<sub>2</sub> and graphene using the weakest link theory,<sup>55</sup> the log–log plots are presented in Figure 6 (larger slope of the curve reflects stronger dependence) with the corresponding fitting line parameters shown in Table S2, SI. As seen in Figure 6, the strength and Young's moduli of MXenes exhibit a much weaker dependence on the number of monolayers in a stack in comparison to MoS<sub>2</sub> and graphene. A rapid decrease in the mechanical properties of multilayer MoS<sub>2</sub> implies a significant degradation of the material structure with more layers. By contrast, the MXenes used in our study display

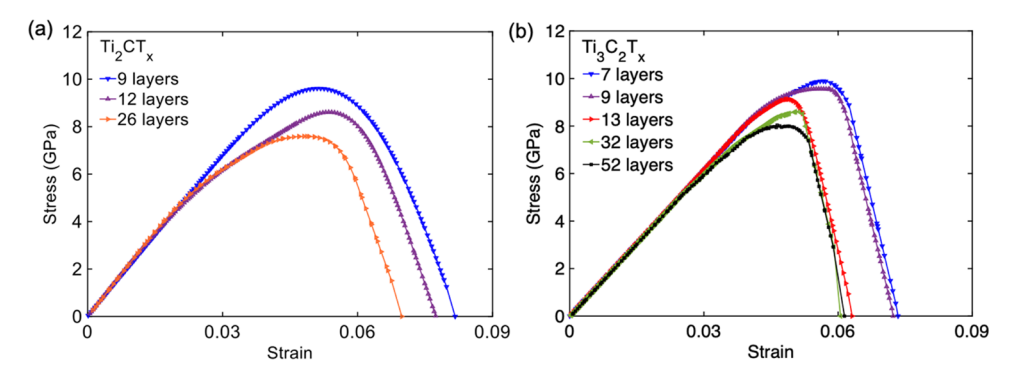


Figure 5. Stress-strain curves for (a) Ti<sub>2</sub>CT<sub>x</sub> and (b) Ti<sub>3</sub>C<sub>2</sub>T<sub>x</sub> samples.

Table 1. Strength  $(\sigma_m)$  and Young's Modulus (E) of  $Ti_2CT_x$  and  $Ti_3C_2T_x$  Films with a Number of Monolayers (n) in the Stack

material	method	n	$\sigma_{\mathrm{m}}$ (GPa)	E (GPa)
Ti <sub>2</sub> CT <sub>x</sub>	experiment	9	9.61	217.15
		12	8.61	218.68
		26	7.59	217.44
	MD modeling	1	11.66	265.91
		3	11.35	259.99
		5	11.09	263.43
		7	10.80	266.26
		9	10.59	265.54
${ m Ti}_3{ m C}_2{ m T}_x$	experiment	7	9.89	203.40
		9	9.55	207.01
		13	9.22	204.85
		32	8.59	204.96
		52	7.99	204.39
	MD modeling	1	12.47	256.56
		3	11.26	255.18
		5	10.87	255.91
		7	10.59	254.36

much less pronounced reduction in mechanical properties with an increased number of monolayers in the stack.

Atomistic Modeling and Defect Tolerance. Atomistic Modeling of Uniaxially Strained Multilayer MXenes. To reveal the underlying failure mechanism from the obtained experimental results, we conducted a series of molecular dynamics (MD) in silico experiments, in which MXenes were subjected to uniaxial tensile stress. In the MD simulations, we considered the effects of defects, terminal groups, and interlayer interactions. The simulations were conducted using

LAMMPS<sup>40,56</sup> and ReaxFF force fields for MXenes<sup>57,58</sup> with different numbers of monolayers in a stack. The atomic vacancies (missing Ti and C atoms in Figure 7) were created by the removal of Ti or C atoms from the lattice<sup>50</sup> (details in the Materials and Methods section). Similar vacancies created during material synthesis using etching have been reported before. 51 In our MD models, the overall vacancy ratio, defined as the ratio of the number of missing atoms to the total number of atoms in a monolayer, was kept at  $3.0 \pm 0.5\%$ . Accordingly, in a multilayer system, the vacancy ratio among different layers randomly deviates from the mean within the standard deviation, as shown in Table S3, SI. In addition, the terminating -O- and -F atoms were added randomly to the models (8.0  $\pm$  0.9% of -O-terminating groups and 3.0  $\pm$  0.5% of -F-terminating groups with respect to the total number of Ti and C atoms in a monolayer according to the experimental XPS results<sup>46</sup> (Figure S1c, SI) for a 6.0  $\mu$ m × 6.0  $\mu$ m sampling

In our typical MD simulation, the system is uniaxially stretched at 298 K along the zigzag direction in an NVT ensemble with a Nosé–Hoover thermostat. MD simulations differ from the experiments in many aspects, including a simplified material model and a  $10^3-10^4$  times higher loading rate. Nevertheless, the stress–strain relationships (Figure 8a,b) obtained from MD exhibit behavior similar to the experiment. To understand the deformation and failure mechanism, a series of snapshots of the atomistic systems were taken along the loading path, as shown in Figure 8c,d. The layer-by-layer strain contours for all MD modeling cases are illustrated in Figures S4–S18, SI. Color in these snapshots encodes the strain on atoms, calculated as  $\varepsilon = \frac{1}{6} \sum_{i=1}^{6} \frac{y_{ii} - y_{io}}{y_{io}}$ , where  $y_{io}$  and  $y_{if}$  are the

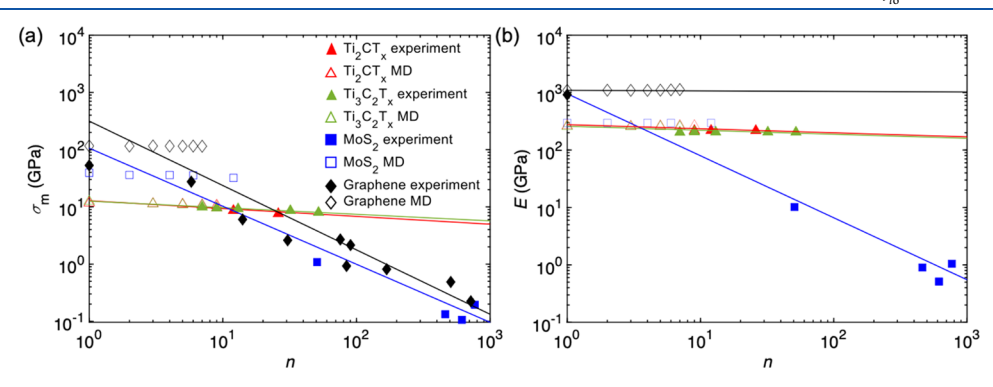


Figure 6. Log-log plots of (a) strength and (b) Young's modulus as a function of the number of monolayers in a stack for different materials (listed in the legend in (a)). Literature data for  $MoS_2^{52}$  and graphene<sup>53,54</sup> are shown for comparison.

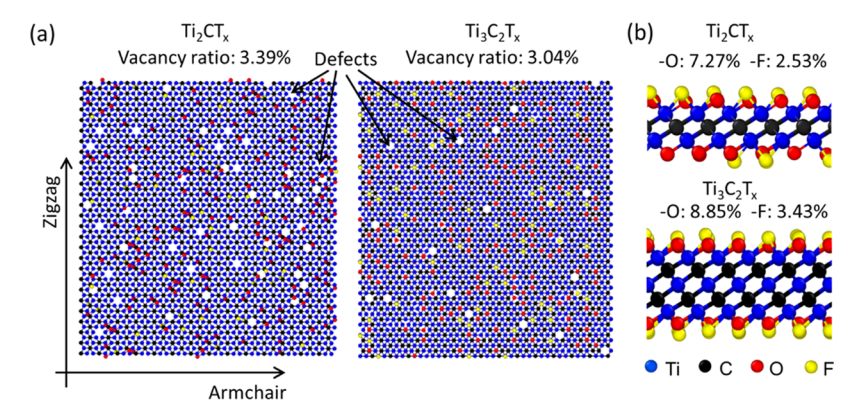


Figure 7. (a) Top and (b) side views of  $Ti_2CT_x$  and  $Ti_3C_2T_x$  monolayers (7.5 nm  $\times$  8.0 nm). Load was applied along the zigzag direction.

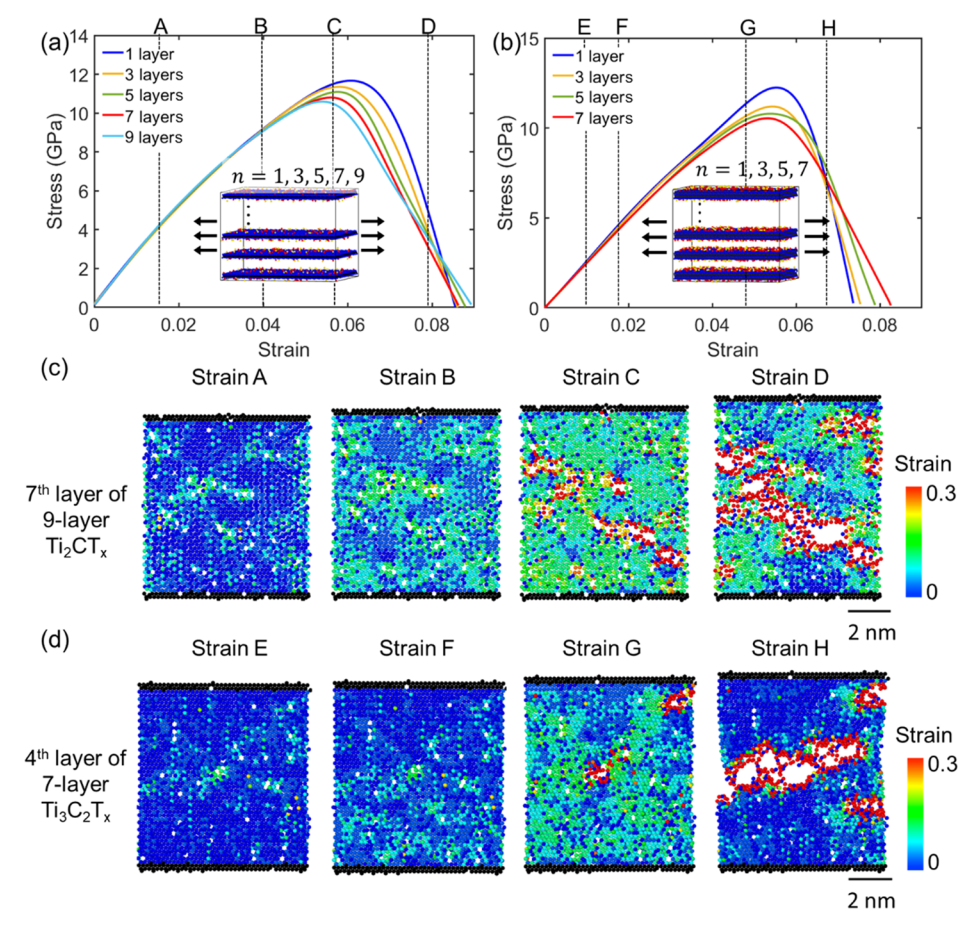


Figure 8. MD stress versus strain curves for (a)  $Ti_2CT_x$  and (b)  $Ti_3C_2T_x$ . Insets show geometry and loading settings for the multilayer MXenes. (c, d) MD snapshots of the weakest MXene layer (7.5 nm × 8.0 nm) in a stack, showing the material at the average strain per atom in critical points indicated in (a) and (b).

original and final distances along the loading direction between the atom of interest and its *i*th neighboring carbon atom (six carbon atoms are considered as neighbors in an example in Figure S19, SI).

In the initial elastic stage, the monolayer and multilayer systems display similar distributions of strain, where the interatomic bonds experience larger deformations near the vacancies compared to pristine regions. The observed earlier crack initiation in the multilayered structure compared to the monolayer structure is a consequence of statistical variation in the number of vacancies among the stacked layers. Although the average vacancy ratio in our simulations was 3.0%, it

slightly varied from monolayer to monolayer within  $\pm 0.5\%$ . With these variations, it is natural that a chance of encountering a monolayer with a larger-than-average vacancy ratio in a stack is higher when the stack is formed by a larger number of the monolayers. Such a more defected monolayer represents the weakest link in the stack and shows earlier crack initiation compared to other monolayers in the stack, as well as to those individual monolayer models that have a lower vacancy ratio. This is illustrated in Figure 8c,d (cartoons C and G) for both MXenes. In the multilayer system, the crack nucleates and propagates nonuniformly among different layers mainly due to their different defect densities. The crack

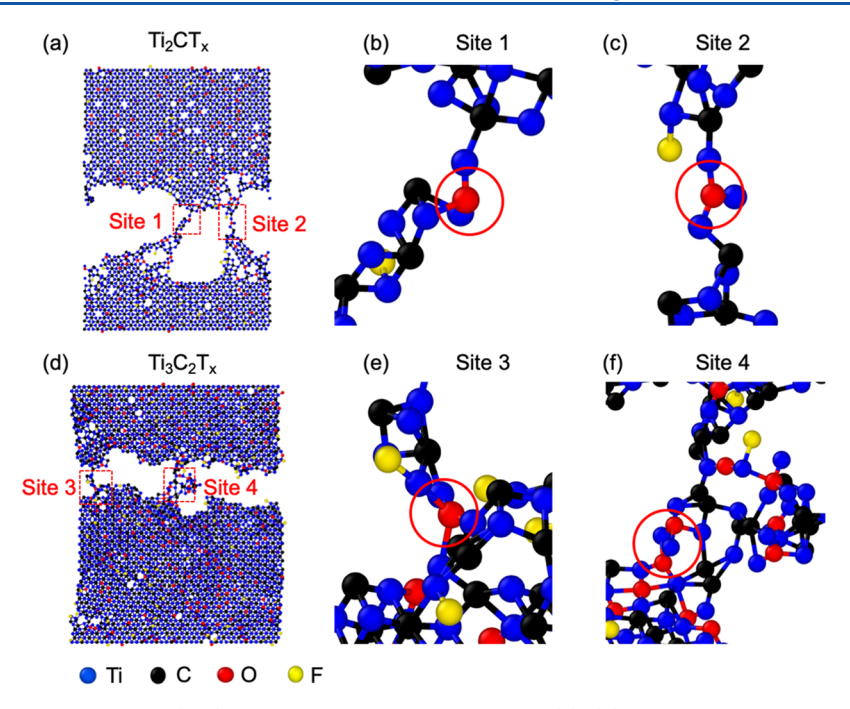


Figure 9. (a) Monolayer  $Ti_2CT_x$  after failure. (b, c) Zoom-ins of the areas indicated in (a). (d) Monolayer  $Ti_3C_2T_x$  after failure. (e, f) Zoom-ins of the areas indicated in (d).

propagation in the weakest layer promotes softening in the stress—strain curve and leads to a reduced strength as the number of monolayers increases. As the load increases, the cracks nucleate and propagate across different layers until a final rupture of the sample. We believe that the statistical variation in the vacancy ratio between different monolayers is the main reason for the observed number-of-layer dependence of strength in the studied MXenes.

Young's modulus and strength obtained from MD simulations are listed in Table 1 and plotted in Figure 6 as a function of the number of monolayers in a stack (n). Similar to the experimental measurements, the modulus is independent on n, while the strength decreases with the increasing number of monolayers. It is also shown in Table 1 that there is a discrepancy between simulation results and experimental results for both MXenes, which is mainly due to different time and length scales implemented in the MD modeling. However, the main purpose of the MD modeling is to provide more insights with regard to the failure mechanisms rather than exactly reproduce the values of mechanical properties measured in the experiment. Direct comparison between strength and modulus values is not the main goal of this work. In the same figure, we also plotted literature results for multilayer MoS<sub>2</sub><sup>52</sup> and graphene, <sup>59</sup> obtained from simulations in which the material defects were not considered. In contrast to our modeling results for the MXenes, the strength calculated from those simulations does not show any dependence on the number of monolayers in a stack. Based on this comparison, it is evident that defects and their statistical variation in monolayers making up the stack of a layered material play an important role in the overall mechanical behavior of the stack.

Nanocrack Bridging Due to Surface Terminating Groups. In addition, we discuss a specific failure mechanism of the MXenes revealed from MD simulations. Atomic images shown in Figures 8c,d and S4–S18 show that the nanocracks in the MXenes are often bridged by the –O-containing chains

originating from the surface functional groups on MXenes. This bridging effect is more clearly seen in Figure 9, where the crack is bridged by two chains, in which the O atoms play an essential role by connecting two or more Ti atoms. When Ti—C bonds within MXene layers start to fail, the strong interaction between O and Ti atoms results in new Ti—O bonds. This bridging effect may increase the ductility and toughness of MXene. As a result, both the simulation and experiment display a ductile fracture to some extent, in contrast to clean brittle failure observed in other 2D materials such as graphene. It is worth noting here that no bridging was observed in our prior MD simulations of stretching of MXene without terminating groups, 1 pointing out to an interesting role played by surface functional groups in mechanical behavior and failure mechanisms of MXenes.

Scaling Effect on the Strength of MXenes. From the experimental and modeling results, we found that the strength of MXene stacks decreased with the increasing number of monolayers. We also compared the trend of reduction in strength with similar trends for graphene and MoS<sub>2</sub> stacks, as illustrated in Figure 6, from which the MXenes showed a much lower property degradation rate. Combining these experimental observations with the modeling results, we speculate that this is due to two main reasons: (1) relatively larger monolayer thickness of the MXene monolayers compared to other 2D materials and (2) nanocrack bridging induced by the surface terminating groups of MXenes. With a larger monolayer thickness of MXenes, an isolated atomic vacancy has a less dramatic effect on the structural stability of the MXene monolayer, leading to a higher defect tolerance. In contrast, in other 2D materials such as MoS<sub>2</sub> or graphene, a missing Mo or C atom creates a hole through the monolayer rendering it dramatically more vulnerable to fracture. 62-65 In MXenes, the surface Ti atomic vacancies are more common than missing core C vacancies, which allows these materials to retain integrity due to the mainly intact inner C layer even when the outer Ti layers are damaged, resulting in a higher tolerance of a

MXene monolayer to fracture. In addition to the larger monolayer thickness, the nanocrack bridging by functional groups further reduces residual stress at crack edges, which contributes to the higher defect tolerance of MXenes.

### CONCLUSIONS

We present a combined experimental and computational investigation of the in-plane mechanical behavior of stacked MXene films  $(Ti_2CT_r, Ti_3C_2T_r)$ . From the experiment, it is found that Young's modulus exhibits only a small variance when the number of stacked MXene monolayers increases from 9 to 26 for Ti<sub>2</sub>CT<sub>r</sub> and 7 to 52 for Ti<sub>3</sub>C<sub>2</sub>T<sub>r</sub>. At the same time, the tensile strength monotonically decreases from 9.61 to 7.59 GPa (Ti<sub>2</sub>CT<sub>x</sub> with d-spacing of 1.36 nm) and from 9.89 to 7.99 GPa (Ti<sub>3</sub>C<sub>2</sub>T<sub>x</sub> with d-spacing of 1.48 nm). This dependence on the number of stacked monolayers is much weaker than what was previously observed in multilayer graphene and MoS2 films, implying a better scaling-up of mechanical properties of at least the tested MXenes as compared to other multilayer 2D materials. From the atomistic simulations, it is found that the dependence on the number of monolayers in a stack can be attributed to variations in the number of atomic vacancies among different monolayers in the multilayer MXenes. As a result, the cracks are initiated in the weakest layer with the highest defect density, leading to a softening manifested in stress-strain curves and reduced tensile strength. Moreover, MD simulations demonstrated that the cracks in the MXene samples can be bridged by -Oatoms, hindering their propagation and leading to a ductile failure mode. Collectively, these results indicate that MXenes can be excellent reinforcing agents for composite materials across different length scales.

#### ASSOCIATED CONTENT

#### Supporting Information

The Supporting Information is available free of charge at https://pubs.acs.org/doi/10.1021/acsanm.1c00537.

Contrast recognition method (Note S1); Raman spectra, XPS survey, and XRD patterns for MXene films (Figure S1); SEM image of a neat PTP device before application of MXene coating (Figure S2); TEM images of crack edges and contrast recognition, Fourier fitting, first and second derivatives for  $\text{Ti}_2\text{CT}_x$  and  $\text{Ti}_3\text{C}_2\text{T}_x$  (Figure S3); MD modeling strain contours (Figures S4–S18); example of  $\text{Ti}_3\text{C}_2\text{T}_x$  before and after being stretched along the zigzag direction (Figure S19); strength and Young's modulus values for  $\text{MoS}_2$  and graphene (Table S1); fitting parameters for  $\text{lg}(\sigma) = -A \, \text{lg}(n) + B$  based on the experimental results (Table S2); defect ratio (Table S3) (PDF)

In situ tensile testing of nine-layer  $Ti_3C_2T_x$  (Video S1) (MP4)

# AUTHOR INFORMATION

## **Corresponding Authors**

Chenglin Wu — Department of Civil, Architectural, and Environmental Engineering, Missouri University of Science and Technology, Rolla, Missouri 65409, United States;
orcid.org/0000-0001-7733-1084; Email: wuch@mst.edu

Vadym N. Mochalin – Department of Chemistry and Department of Materials Science and Engineering, Missouri University of Science and Technology, Rolla, Missouri 65409, *United States;* orcid.org/0000-0001-7403-1043; Email: mochalinv@mst.edu

#### **Authors**

Yanxiao Li — Department of Civil, Architectural, and Environmental Engineering, Missouri University of Science and Technology, Rolla, Missouri 65409, United States

Congjie Wei – Department of Civil, Architectural, and Environmental Engineering, Missouri University of Science and Technology, Rolla, Missouri 65409, United States

Shuohan Huang – Department of Chemistry, Missouri University of Science and Technology, Rolla, Missouri 65409, United States

Arman Ghasemi — Department of Mechanical Engineering, The University of Texas at San Antonio, San Antonio, Texas 78249, United States

Wei Gao – Department of Mechanical Engineering, The University of Texas at San Antonio, San Antonio, Texas 78249, United States

Complete contact information is available at: https://pubs.acs.org/10.1021/acsanm.1c00537

### **Author Contributions**

<sup>1</sup>Y.L., C.W., and S.H. contributed equally to this work.

#### Notes

The authors declare no competing financial interest.

#### ACKNOWLEDGMENTS

Y. Li, C. Wei, S. Huang, V. N. Mochalin, and C. Wu gratefully acknowledge financial support of this work by the National Science Foundation through Grant no. CMMI-1930881. The authors also acknowledge funding support from the Material Research Center at Missouri University of Science and Technology, Mid-America Transportation Center, and Missouri Department of Transportation. W. Gao and A. Ghasemi gratefully acknowledge financial support of this work by the National Science Foundation through Grant no. CMMI-1930783. The authors acknowledge the Texas Advanced Computing Center (TACC) at the University of Texas at Austin for providing HPC resources that have contributed to the research results reported within this paper.

#### REFERENCES

- (1) Naguib, M.; Kurtoglu, M.; Presser, V.; Lu, J.; Niu, J.; Heon, M.; Hultman, L.; Gogotsi, Y.; Barsoum, M. W. Two-Dimensional Nanocrystals Produced by Exfoliation of Ti<sub>3</sub>AlC<sub>2</sub>. *Adv. Mater.* **2011**, 23, 4248–4253.
- (2) Naguib, M.; Mashtalir, O.; Carle, J.; Presser, V.; Lu, J.; Hultman, L.; Gogotsi, Y.; Barsoum, M. W. Two-Dimensional Transition Metal Carbides. *ACS Nano* **2012**, *6*, 1322–1331.
- (3) Barsoum, M. W. The  $MN_{+1}AX_N$  Phases: A New Class of Solids: Thermodynamically Stable Nanolaminates. *Prog. Solid State Chem.* **2000**, 28, 201–281.
- (4) Naguib, M.; Mochalin, V. N.; Barsoum, M. W.; Gogotsi, Y. 25th Anniversary Article: MXenes: A New Family of Two-Dimensional Materials. *Adv. Mater.* **2014**, *26*, 992–1005.
- (5) Alhabeb, M.; Maleski, K.; Anasori, B.; Lelyukh, P.; Clark, L.; Sin, S.; Gogotsi, Y. Guidelines for Synthesis and Processing of Two-Dimensional Titanium Carbide (Ti<sub>3</sub>C<sub>2</sub>T<sub>x</sub> MXene). *Chem. Mater.* **2017**, *29*, 7633–7644.
- (6) Mashtalir, O.; Naguib, M.; Dyatkin, B.; Gogotsi, Y.; Barsoum, M. W. Kinetics of Aluminum Extraction from Ti<sub>3</sub>AlC<sub>2</sub> in Hydrofluoric Acid. *Mater. Chem. Phys.* **2013**, *139*, 147–152.

- (7) Wang, H.-W.; Naguib, M.; Page, K.; Wesolowski, D. J.; Gogotsi, Y. Resolving the Structure of  ${\rm Ti}_3{\rm C}_2{\rm T}_{\rm x}$  MXenes through Multilevel Structural Modeling of the Atomic Pair Distribution Function. *Chem. Mater.* **2016**, 28, 349–359.
- (8) Mashtalir, O.; Naguib, M.; Mochalin, V. N.; Dall'Agnese, Y.; Heon, M.; Barsoum, M. W.; Gogotsi, Y. Intercalation and Delamination of Layered Carbides and Carbonitrides. *Nat. Commun.* **2013**, *4*, No. 1716.
- (9) Hart, J. L.; Hantanasirisakul, K.; Lang, A. C.; Anasori, B.; Pinto, D.; Pivak, Y.; van Omme, J. T.; May, S. J.; Gogotsi, Y.; Taheri, M. L. Control of MXenes' Electronic Properties through Termination and Intercalation. *Nat. Commun.* **2019**, *10*, No. 522.
- (10) Ling, Z.; Ren, C. E.; Zhao, M.-Q.; Yang, J.; Giammarco, J. M.; Qiu, J.; Barsoum, M. W.; Gogotsi, Y. Flexible and Conductive MXene Films and Nanocomposites with High Capacitance. *Proc. Natl. Acad. Sci. U.S.A.* 2014, 111, 16676–16681.
- (11) Lukatskaya, M. R.; Mashtalir, O.; Ren, C. E.; Dall'Agnese, Y.; Rozier, P.; Taberna, P. L.; Naguib, M.; Simon, P.; Barsoum, M. W.; Gogotsi, Y. Cation Intercalation and High Volumetric Capacitance of Two-Dimensional Titanium Carbide. *Science* **2013**, *341*, 1502–1505.
- (12) Xie, Y.; Naguib, M.; Mochalin, V. N.; Barsoum, M. W.; Gogotsi, Y.; Yu, X.; Nam, K.-W.; Yang, X.-Q.; Kolesnikov, A. I.; Kent, P. R. Role of Surface Structure on Li-Ion Energy Storage Capacity of Two-Dimensional Transition-Metal Carbides. *J. Am. Chem. Soc.* **2014**, *136*, 6385–6394.
- (13) Naguib, M.; Halim, J.; Lu, J.; Cook, K. M.; Hultman, L.; Gogotsi, Y.; Barsoum, M. W. New Two-Dimensional Niobium and Vanadium Carbides As Promising Materials for Li-Ion Batteries. *J. Am. Chem. Soc.* **2013**, *135*, 15966–15969.
- (14) Anasori, B.; Lukatskaya, M. R.; Gogotsi, Y. 2D Metal Carbides and Nitrides (MXenes) for Energy Storage. *Nat. Rev. Mater.* **2017**, 2, No. 16098.
- (15) Ghidiu, M.; Lukatskaya, M. R.; Zhao, M.-Q.; Gogotsi, Y.; Barsoum, M. W. Conductive Two-Dimensional Titanium Carbide 'Clay' with High Volumetric Capacitance. *Nature* **2014**, *516*, 78–81.
- (16) Yi, J.; Li, J.; Huang, S.; Hu, L.; Miao, L.; Zhao, C.; Wen, S.; Mochalin, V. N.; Rao, A. M. Ti<sub>2</sub>CT<sub>x</sub> MXene-Based All-Optical Modulator. *InfoMat* **2020**, *2*, 601–609.
- (17) Dong, Y.; Chertopalov, S.; Maleski, K.; Anasori, B.; Hu, L.; Bhattacharya, S.; Rao, A. M.; Gogotsi, Y.; Mochalin, V. N.; Podila, R. Saturable Absorption in 2D Ti<sub>3</sub>C<sub>2</sub> MXene Thin Films for Passive Photonic Diodes. *Adv. Mater.* **2018**, *30*, No. 1705714.
- (18) Yi, J.; Du, L.; Li, J.; Yang, L.; Hu, L.; Huang, S.; Dong, Y.; Miao, L.; Wen, S.; Mochalin, V. N.; et al. Unleashing the Potential of  ${\rm Ti}_2{\rm CT}_{\rm x}$  MXene As A Pulse Modulator for Mid-Infrared Fiber Lasers. 2D Mater. 2019, 6, No. 045038.
- (19) Hantanasirisakul, K.; Gogotsi, Y. Electronic and Optical Properties of 2D Transition Metal Carbides and Nitrides (MXenes). *Adv. Mater.* **2018**, *30*, No. 1804779.
- (20) Li, G.; Amer, N.; Hafez, H. A.; Huang, S.; Turchinovich, D.; Mochalin, V. N.; Hegmann, F. A.; Titova, L. V. Dynamical Control over Terahertz Electromagnetic Interference Shielding with 2D  $T_{i_3}C_2T_y$  MXene by Ultrafast Optical Pulses. *Nano Lett.* **2020**, 20, 636–643.
- (21) Han, M.; Shuck, C. E.; Rakhmanov, R.; Parchment, D.; Anasori, B.; Koo, C. M.; Friedman, G.; Gogotsi, Y. Beyond Ti<sub>3</sub>C<sub>2</sub>T<sub>x</sub>: MXenes for Electromagnetic Interference Shielding. *ACS Nano* **2020**, *14*, 5008–5016
- (22) Shahzad, F.; Alhabeb, M.; Hatter, C. B.; Anasori, B.; Hong, S. M.; Koo, C. M.; Gogotsi, Y. Electromagnetic Interference Shielding with 2D Transition Metal Carbides (MXenes). *Science* **2016**, 353, 1137–1140.
- (23) Li, Z.; Wu, Y. 2D Early Transition Metal Carbides (MXenes) for Catalysis. *Small* **2019**, *15*, No. 1804736.
- (24) Blanco, E.; Rosenkranz, A.; Espinoza-González, R.; Fuenzalida, V. M.; Zhang, Z.; Suárez, S.; Escalona, N. Catalytic Performance of 2D-MXene Nano-Sheets for the Hydrodeoxygenation (HDO) of Lignin-Derived Model Compounds. *Catal. Commun.* **2020**, *133*, No. 105833.

- (25) Gouveia, J. D.; Morales-García, A.; Viñes, F.; Illas, F.; Gomes, J. R. MXenes As Promising Catalysts for Water Dissociation. *Appl. Catal., B* **2020**, *260*, No. 118191.
- (26) Hou, T.; Luo, Q.; Li, Q.; Zu, H.; Cui, P.; Chen, S.; Lin, Y.; Chen, J.; Zheng, X.; Zhu, W.; et al. Modulating Oxygen Coverage of Ti<sub>3</sub>C<sub>2</sub>T<sub>x</sub> MXenes to Boost Catalytic Activity for HCOOH Dehydrogenation. *Nat. Commun.* **2020**, *11*, No. 4251.
- (27) Kim, S. J.; Koh, H.-J.; Ren, C. E.; Kwon, O.; Maleski, K.; Cho, S.-Y.; Anasori, B.; Kim, C.-K.; Choi, Y.-K.; Kim, J.; et al. Metallic  ${\rm Ti}_3{\rm C}_2{\rm T}_{\rm x}$  MXene Gas Sensors with Ultrahigh Signal-to-Noise Ratio. *ACS Nano* **2018**, *12*, 986–993.
- (28) Muckley, E. S.; Naguib, M.; Wang, H.-W.; Vlcek, L.; Osti, N. C.; Sacci, R. L.; Sang, X.; Unocic, R. R.; Xie, Y.; Tyagi, M.; et al. Multimodality of Structural, Electrical, and Gravimetric Responses of Intercalated MXenes to Water. *ACS Nano* **2017**, *11*, 11118–11126.
- (29) Chertopalov, S.; Mochalin, V. N. Environment-Sensitive Photoresponse of Spontaneously Partially Oxidized Ti<sub>3</sub>C<sub>2</sub> MXene Thin Films. *ACS Nano* **2018**, *12*, 6109–6116.
- (30) Mojtabavi, M.; VahidMohammadi, A.; Liang, W.; Beidaghi, M.; Wanunu, M. Single-Molecule Sensing Using Nanopores in Two-Dimensional Transition Metal Carbide (MXene) Membranes. *ACS Nano* **2019**, *13*, 3042–3053.
- (31) Huang, S.; Mutyala, K.; Sumant, A.; Mochalin, V. Achieving Superlubricity with 2D Transition Metal Carbides (MXenes) and MXene/Graphene Coatings. *Mater. Today Adv.* **2021**, *9*, No. 100133.
- (32) Grützmacher, P. G.; Suarez, S.; Tolosa, A.; Gachot, C.; Song, G.; Wang, B.; Presser, V.; Mücklich, F.; Anasori, B.; Rosenkranz, A. Superior Wear-Resistance of  ${\rm Ti_3C_2T_x}$  Multilayer Coatings. *ACS Nano* **2021**, DOI: 10.1021/acsnano.1c01555.
- (33) Zhan, X.; Si, C.; Zhou, J.; Sun, Z. MXene and MXene-Based Composites: Synthesis, Properties and Environment-Related Applications. *Nanoscale Horiz.* **2020**, *5*, 235–258.
- (34) Monastyreckis, G.; Mishnaevsky, L., Jr.; Hatter, C.; Aniskevich, A.; Gogotsi, Y.; Zeleniakiene, D. Micromechanical Modeling of MXene-Polymer Composites. *Carbon* **2020**, *162*, 402–409.
- (35) Riazi, H.; Nemani, S. K.; Grady, M. C.; Anasori, B.; Soroush, M. Ti<sub>3</sub>C<sub>2</sub> MXene–Polymer Nanocomposites and Their Applications. *J. Mater. Chem. A* **2021**, *9*, 8051–8098.
- (36) Hong, W.; Wyatt, B. C.; Nemani, S. K.; Anasori, B. Double Transition-Metal MXenes: Atomistic Design of Two-Dimensional Carbides and Nitrides. *MRS Bull.* **2020**, *45*, 850–861.
- (37) Lipatov, A.; Lu, H.; Alhabeb, M.; Anasori, B.; Gruverman, A.; Gogotsi, Y.; Sinitskii, A. Elastic Properties of 2D  ${\rm Ti_3}C_2{\rm T_x}$  MXene Monolayers and Bilayers. *Sci. Adv.* **2018**, *4*, No. eaat0491.
- (38) Yorulmaz, U.; Özden, A.; Perkgöz, N. K.; Ay, F.; Sevik, C. Vibrational and Mechanical Properties of Single Layer MXene Structures: A First-Principles Investigation. *Nanotechnology* **2016**, 27, No. 335702.
- (39) Zha, X.-H.; Luo, K.; Li, Q.; Huang, Q.; He, J.; Wen, X.; Du, S. Role of The Surface Effect on The Structural, Electronic and Mechanical Properties of The Carbide MXenes. *EPL* **2015**, *111*, No. 26007.
- (40) Borysiuk, V. N.; Mochalin, V. N.; Gogotsi, Y. Molecular Dynamic Study of The Mechanical Properties of Two-Dimensional Titanium Carbides  ${\rm Ti}_{n+1}{\rm C}_n$  (MXenes). Nanotechnology **2015**, 26, No. 265705.
- (41) Luo, S.; Patole, S. P.; Anwer, S.; Li, B.; Delclos, T.; Gogotsi, O.; Zahorodna, V.; Balitskyi, V.; Liao, K. Tensile behaviors of  $Ti_3C_2T_x$  (MXene) films. *Nanotechnology* **2020**, *31*, No. 395704.
- (42) Firestein, K. L.; von Treifeldt, J. E.; Kvashnin, D. G.; Fernando, J. F.; Zhang, C.; Kvashnin, A. G.; Podryabinkin, E. V.; Shapeev, A. V.; Siriwardena, D. P.; Sorokin, P. B.; Golberg, D. Young's Modulus and Tensile Strength of Ti<sub>3</sub>C<sub>2</sub> MXene Nanosheets As Revealed by in situ TEM Probing, AFM Nanomechanical Mapping and Theoretical Calculations. *Nano Lett.* **2020**, *20*, 5900–5908.
- (43) Borysiuk, V. N.; Mochalin, V. N.; Gogotsi, Y. Bending Rigidity of Two-Dimensional Titanium Carbide (MXene) Nanoribbons: A Molecular Dynamics Study. *Comput. Mater. Sci.* **2018**, *143*, 418–424.

- (44) Koenig, S. P.; Boddeti, N. G.; Dunn, M. L.; Bunch, J. S. Ultrastrong Adhesion of Graphene Membranes. *Nat. Nanotechnol.* **2011**, *6*, 543.
- (45) Gong, P.; Li, Q.; Liu, X.-Z.; Carpick, R. W.; Egberts, P. Adhesion Mechanics between Nanoscale Silicon Oxide Tips and Few-Layer Graphene. *Tribol. Lett.* **2017**, *65*, No. 61.
- (46) Li, Y.; Huang, S.; Wei, C.; Wu, C.; Mochalin, V. N. Adhesion of Two-Dimensional Titanium Carbides (MXenes) and Graphene to Silicon. *Nat. Commun.* **2019**, *10*, No. 3014.
- (47) Huang, S.; Mochalin, V. N. Hydrolysis of 2D Transition-Metal Carbides (MXenes) in Colloidal Solutions. *Inorg. Chem.* **2019**, *58*, 1958–1966.
- (48) Stukowski, A. Visualization and Analysis of Atomistic Simulation Data with OVITO—the Open Visualization Tool. *Modell. Simul. Mater. Sci. Eng.* **2009**, *18*, No. 015012.
- (49) Kim, Y.; Lee, S.; Lim, J.; Weon, B. M. X-Ray Nanotomography of Dry Colloidal Packings. Sci. Rep. 2020, 10, No. 17222.
- (50) Noshin, M.; Khan, A. I.; Navid, I. A.; Uddin, H. A.; Subrina, S. Impact of Vacancies on The Thermal Conductivity of Graphene Nanoribbons: A Molecular Dynamics Simulation Study. *AIP Adv.* **2017**, 7, No. 015112.
- (51) Sang, X.; Xie, Y.; Lin, M.-W.; Alhabeb, M.; Van Aken, K. L.; Gogotsi, Y.; Kent, P. R.; Xiao, K.; Unocic, R. R. Atomic Defects in Monolayer Titanium Carbide  $(\mathrm{Ti}_3\mathrm{C}_2\mathrm{T}_{\mathrm{x}})$  MXene. *ACS Nano* **2016**, *10*, 9193–9200.
- (52) Li, P.; Jiang, C.; Xu, S.; Zhuang, Y.; Gao, L.; Hu, A.; Wang, H.; Lu, Y. *In situ* Nanomechanical Characterization of Multi-Layer MoS<sub>2</sub> Membranes: from Intraplanar to Interplanar Fracture. *Nanoscale* **2017**, *9*, 9119–9128.
- (53) Li, P.; Cao, K.; Jiang, C.; Xu, S.; Gao, L.; Xiao, X.; Lu, Y. In Situ Tensile Fracturing of Multilayer Graphene Nanosheets for Their in-Plane Mechanical Properties. *Nanotechnology* **2019**, *30*, No. 475708.
- (54) Cao, K.; Feng, S.; Han, Y.; Gao, L.; Ly, T. H.; Xu, Z.; Lu, Y. Elastic Straining of Free-Standing Monolayer Graphene. *Nat. Commun.* **2020**, *11*, No. 284.
- (55) Lei, W.-S. A Generalized Weakest-Link Model for Size Effect on Strength of Quasi-Brittle Materials. *J. Mater. Sci.* **2018**, 53, 1227–1245.
- (56) Plimpton, S. Fast Parallel Algorithms for Short-Range Molecular Dynamics. *J. Comput. Phys.* **1995**, *117*, 1–19.
- (57) Huygh, S.; Bogaerts, A.; van Duin, A. C.; Neyts, E. C. Development of A ReaxFF Reactive Force Field for Intrinsic Point Defects in Titanium Dioxide. *Comput. Mater. Sci.* **2014**, *95*, 579–591.
- (58) Lotfi, R.; Naguib, M.; Yilmaz, D. E.; Nanda, J.; Van Duin, A. C. A Comparative Study on The Oxidation of Two-Dimensional Ti<sub>3</sub>C<sub>2</sub> MXene Structures in Different Environments. *J. Mater. Chem. A* **2018**, *6*, 12733–12743.
- (59) Zhang, Y. Y.; Gu, Y. Mechanical Properties of Graphene: Effects of Layer Number, Temperature and Isotope. *Comput. Mater. Sci.* **2013**, *71*, 197–200.
- (60) Zhang, P.; Ma, L.; Fan, F.; Zeng, Z.; Peng, C.; Loya, P. E.; Liu, Z.; Gong, Y.; Zhang, J.; Zhang, X.; et al. Fracture Toughness of Graphene. *Nat. Commun.* **2014**, *5*, No. 3782.
- (61) Wei, C.; Wu, C. Nonlinear Fracture of Two-Dimensional Transitional Metal Carbides (MXenes). *Eng. Fract. Mech.* **2020**, 230, No. 106978.
- (62) Zhou, W.; Zou, X.; Najmaei, S.; Liu, Z.; Shi, Y.; Kong, J.; Lou, J.; Ajayan, P. M.; Yakobson, B. I.; Idrobo, J.-C. Intrinsic Structural Defects in Monolayer Molybdenum Disulfide. *Nano Lett.* **2013**, *13*, 2615–2622.
- (63) Wang, S.; Qin, Z.; Jung, G. S.; Martin-Martinez, F. J.; Zhang, K.; Buehler, M. J.; Warner, J. H. Atomically Sharp Crack Tips in Monolayer MoS<sub>2</sub> and Their Enhanced Toughness by Vacancy Defects. *ACS Nano* **2016**, *10*, 9831–9839.
- (64) Liu, Y.; Chen, X. Mechanical Properties of Nanoporous Graphene Membrane. J. Appl. Phys. 2014, 115, No. 034303.
- (65) Agius Anastasi, A.; Ritos, K.; Cassar, G.; Borg, M. K. Mechanical Properties of Pristine and Nanoporous Graphene. *Mol. Simul.* **2016**, 42, 1502–1511.